Intelligent PV Power System With Unbalanced Current Compensation Using CFNN-AMF

Faa-Jeng Lin, *Fellow, IEEE*, Kuang-Hsiung Tan, Yu-Kai Lai, and Wen-Chou Luo

***Abstract*—A novel method is proposed to compensate the three-phase unbalanced currents of power grid under three-phase unbalanced load for a two-stage photovoltaic (PV) power system without the augmentation of active power filter. The PV power system is composed of an interleaved dc/dc converter and a three-level neutral-point clamped inverter. Moreover, the PV power system possesses the smart inverter function, in which the output active and reactive powers of the PV inverter are predetermined by a power factor according to grid codes of the utilities. In the proposed method, $dq0$-axis compensation currents are obtained through low-pass filters to compensate the three-phase unbalanced currents of power grid. Furthermore, in order to improve the control performance of the dc bus voltage of the PV power system under unbalanced load variation condition, an online-trained compensatory neural fuzzy network with an asymmetric membership function (CFNN-AMF) is proposed to replace the traditional proportional-integral controller for the dc bus voltage control. In the proposed CFNN-AMF, the compensatory parameter to integrate pessimistic and optimistic operations of fuzzy systems is embedded in the CFNN. In addition, the dimensions of the Gaussian membership functions are directly extended to AMFs. Additionally, the proposed controllers of the PV power system are implemented by two control platforms using floating-point digital signal processor. Finally, excellent compensation performance for the three-phase currents of power grid under three-phase unbalanced load can be achieved from the experimental results.**

***Index Terms*—Asymmetric membership function (AMF), compensatory neural fuzzy network (CFNN), interleaved dc/dc converter, photovoltaic (PV) power system, smart inverter, three-level neutral-point clamped (NPC) inverter, unbalanced current compensation.**

I. Introduction

SINCE the large amount connection of distributed energy sources (DESs) can introduce a negative impact on the stability and reliability of the power grid, there are more and more grid codes demanding DESs to imitate the conventional power plants to inject or absorb reactive power to support the stability

Manuscript received June 11, 2018; revised October 28, 2018; accepted December 7, 2018. Date of publication December 19, 2018; date of current version June 10, 2019. This work was supported by the Ministry of Science and Technology of Taiwan under Grant MOST 106-2221-E-008-049-MY3. Recommended for publication by Associate Editor C. A. Canesin. *(Corresponding author: Faa-Jeng Lin.)*

F.-J. Lin, Y.-K. Lai, and W.-C. Luo are with the Department of Electrical Engineering, National Central University, Taoyuan 32001, Taiwan (e-mail:

power quality [9]–[12]. Owing to its simplified structure, the shunt APF has become the most widely employed type [13]–[15]. In order to compensate load harmonic currents, a shunt APF is directly connected with the power grid and loads in parallel, and is used to generate compensation currents [13]–[15]. Moreover, since the control algorithm of the APF will cause a large amount of apparent power, which includes the active power for the losses and reactive power for the capacitor, flowing into or out of the APF, a dc bus capacitor is required on the dc side of the APF to release or absorb the apparent power [16], [17]. Therefore, the regulation control of the dc bus voltage of the APF is important especially under the load variation condition. However, traditional proportional-integral (PI) controller has been adopted for the dc bus voltage regulation control only resulted in sluggish responses [16], [17].

The current grid-connected PV power system lacking the capability to deal with the power pollution in the grid, which is resulted from nonlinear and unbalanced loads. However, the augmentation of the APF will increase the cost and size of the PV power system. Therefore, a novel method is proposed in this study to compensate the three-phase unbalanced grid currents under three-phase unbalanced load in grid-connected operation for a two-stage PV power system without the augmentation of APF. The PV power system is composed of an interleaved dc/dc converter [18], [19] and a three-level neutral-point clamped (NPC) inverter [20]. In the proposed method, the $dq0$-axis harmonic currents are augmented to the dc bus voltage controller for active power controller, reactive power controller, and dc bus voltage balancing controller, respectively, to compensate the three-phase unbalanced currents. Moreover, in order to improve the control performance of the dc bus voltage of the PV power system under unbalanced load variation condition, an online-trained CFNN-AMF is proposed to replace the PI controller for the dc bus voltage control. In the proposed CFNN-AMF, not only the compensatory parameter to integrate pessimistic and optimistic operations of fuzzy systems is embedded in the CFNN, but also the dimensions of the Gaussian membership functions are directly extended to AMFs. Furthermore, a BP-based online training algorithm is derived to train the connective weights and parameters of the membership functions of the proposed online CFNN-AMF. In addition, the proposed controllers for the PV power system are implemented by two control platforms using the Texas Instruments (TI) floating-point digital signal processor (DSP) TMS320F28335. In this study, the operating theories of the PV power system with the three-phase unbalanced grid currents compensation will be introduced in Section II. The network structure and online learning algorithms of the proposed CFNN-AMF will be described in Section III. Then, the detailed implementation of the intelligent CFNN-AMF-controlled PV power system will be presented in Section IV. Finally, the conclusions can be found in Section V.

II. PV Power System

In this study, a PV power system with two-stage circuit architecture is developed as shown in Fig. 1. The first stage is an interleaved dc/dc converter shown in Fig. 1(a) [18], [19] and is responsible for the power transmission from the PV panel terminal to the dc bus. The second stage is a three-level NPC inverter shown in Fig. 1(b) [20] and is responsible for the power transmission from the dc bus to the three-phase grid system. In Fig. 1(a) and (b), mode I is the maximum power point tracking (MPPT) mode, and mode II is the smart inverter mode, in which the output active and reactive powers of the PV inverter are predetermined by a power factor according to grid codes of the utilities.

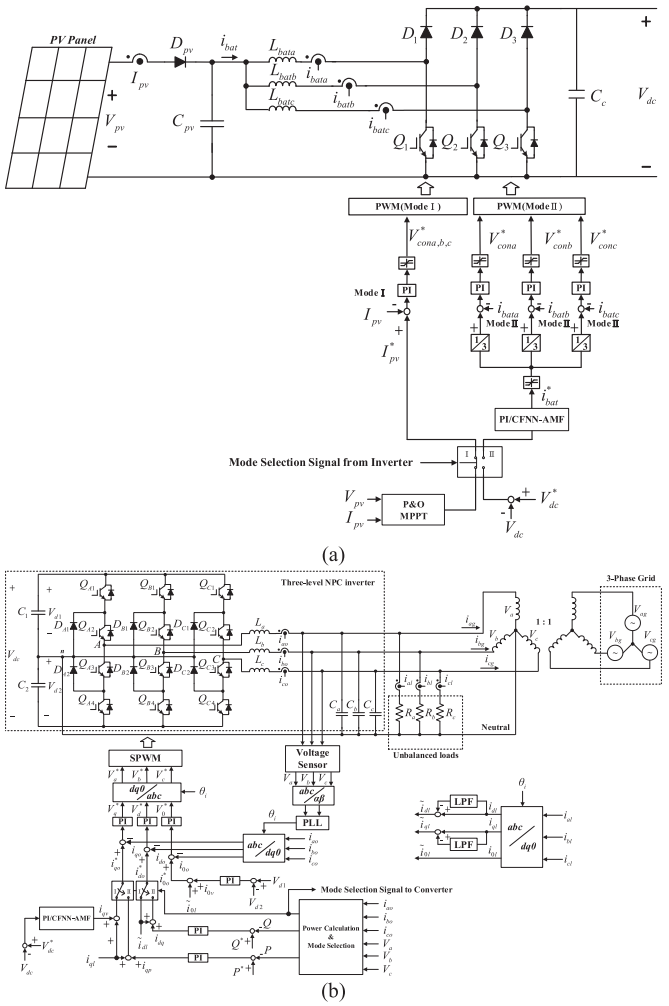

Fig. 1. Block diagrams of a PV system. (a) Interleaved dc/dc converter. (b) Three-Level NPC inverter.

In Fig. 1(a), $V_{\rm pv}$ is the voltage of the PV panel; $I_{\rm pv}$ is the current of the PV panel; $C_{\rm pv}$ is the input capacitor of the dc/dc converter; $i_{{\rm bat}\,a}$, $i_{{\rm bat}\,b}$, and $i_{{\rm bat}\,c}$ are inductors of the dc/dc converter; D_1, D_2, and D_3 are diodes of the dc/dc converter; Q_1, Q_2, and Q_3 are insulated-gate bipolar transistors (IGBTs) of the dc/dc converter; C_c is the capacitor of the dc bus; $i^*_{\rm bat}$ and $i_{{\rm bat}\,a}$, $i_{{\rm bat}\,b}$, $i_{{\rm bat}\,c}$ are the input current command and converter input currents of the dc/dc converter; $I^*_{\rm pv}$ is the maximum current command of the PV panel; $V^*_{\rm dc}$ and $V_{\rm dc}$ are the dc bus voltage command and dc bus voltage; $V^*_{{\rm con}\,a,b,c}$ is the pulsewidth

modulation (PWM) signal at mode I; $V^*_{\text{con }a}$, $V^*_{\text{con }b}$, and $V^*_{\text{con }c}$ are the PWM signals at mode II. In Fig. 1(b), C_1 and C_2 are capacitors of the dc bus; Q_{A1}–Q_{A4}, Q_{B1}–Q_{B4}, and Q_{C1}–Q_{C4} are IGBTs of the dc/ac inverter; D_{A1}, D_{A2}, D_{B1}, D_{B2}, D_{C1}, and D_{C2} are clamped diodes of the dc/ac inverter; L_a, L_b, and L_c are filter inductors of the dc/ac inverter; C_a, C_b, and C_c are filter capacitors of the dc/ac inverter; R_a, R_b, and R_c are the three-phase unbalanced loads; V_{d1} and V_{d2} are the half high voltage and half low voltage of the dc bus voltage; i_{ao}, i_{bo}, and i_{co} are the three-phase currents of the dc/ac inverter; i_{al}, i_{bl}, and i_{cl} are the three-phase currents of the unbalanced loads; i_{ag}, i_{bg}, and i_{cg} are the three-phase currents of the grid; v_{ag}, v_{bg}, and v_{cg} are the three-phase voltages of the grid; V_a, V_b, and V_c are the three-phase voltages of the dc/ac inverter, which are also the three-phase voltages of the primary side of the three-phase Y-Y transformer as shown in Fig. 1(b); θ_i is the synchronous angle obtained from the phase-locked loop; V^*_a, V^*_b, and V^*_c are the three-phase voltage commands of the dc/ac inverter for the sinusoidal PWM (SPWM); V^*_d, V^*_q, and V^*_0 are the $dq0$-axis SPWM voltage commands of the dc/ac inverter; i_{qv} is the dc bus current command; i^*_{do}, i^*_{qo}, i^*_{0o} and i_{do}, i_{qo}, i_{0o} are the $dq0$-axis current commands and $dq0$-axis currents of the dc/ac inverter; P and Q are the active and reactive powers; P^* and Q^* are the active and reactive power commands; i_{qp} is the active current command; i_{dq} is the reactive current command; i_{0v} is the current command for the balance of the dc bus half voltages V_{d1} and V_{d2}; i_{dl}, i_{ql}, and i_{0l} are the $dq0$-axis currents of the unbalanced load; and $\tilde{i}_{dl}$, $\tilde{i}_{ql}$, and $\tilde{i}_{0l}$ are the $dq0$-axis compensated currents of the unbalanced load. The axis conversion between the i_{ao}, i_{bo}, i_{co} and i_{do}, i_{qo}, i_{0o}, V^*_d, V^*_q, V^*_0 and V^*_a, V^*_b, V^*_c, and i_{al}, i_{bl}, i_{cl} and i_{dl}, i_{ql}, i_{0l} are shown in the following:

$$\begin{bmatrix} i_{do} \\ i_{qo} \\ i_{0o} \end{bmatrix} = \frac{2}{3} \begin{bmatrix} \cos\theta_i & \cos\left(\theta_i - \frac{2\pi}{3}\right) & \cos\left(\theta_i + \frac{2\pi}{3}\right) \\ \sin\theta_i & \sin\left(\theta_i - \frac{2\pi}{3}\right) & \sin\left(\theta_i + \frac{2\pi}{3}\right) \\ \frac{1}{2} & \frac{1}{2} & \frac{1}{2} \end{bmatrix} \begin{bmatrix} i_{ao} \\ i_{bo} \\ i_{co} \end{bmatrix} \tag{1}$$

$$\begin{bmatrix} V^*_a \\ V^*_b \\ V^*_c \end{bmatrix} = \begin{bmatrix} \cos\theta_i & \sin\theta_i & 1 \\ \cos\left(\theta_i - \frac{2\pi}{3}\right) & \sin\left(\theta_i - \frac{2\pi}{3}\right) & 1 \\ \cos\left(\theta_i + \frac{2\pi}{3}\right) & \sin\left(\theta_i + \frac{2\pi}{3}\right) & 1 \end{bmatrix} \begin{bmatrix} V^*_q \\ V^*_d \\ V^*_0 \end{bmatrix} \tag{2}$$

$$\begin{bmatrix} i_{dl} \\ i_{ql} \\ i_{0l} \end{bmatrix} = \frac{2}{3} \begin{bmatrix} \cos\theta_i & \cos\left(\theta_i - \frac{2\pi}{3}\right) & \cos\left(\theta_i + \frac{2\pi}{3}\right) \\ \sin\theta_i & \sin\left(\theta_i - \frac{2\pi}{3}\right) & \sin\left(\theta_i + \frac{2\pi}{3}\right) \\ \frac{1}{2} & \frac{1}{2} & \frac{1}{2} \end{bmatrix} \begin{bmatrix} i_{al} \\ i_{bl} \\ i_{cl} \end{bmatrix}. \tag{3}$$

For the interleaved dc–dc converter, in mode I, the perturb and observe method is adopted for the MPPT. The difference of the I^*_{pv} and I_{pv} is regulated by a PI controller to produce the control signal command $V^*_{\text{con }a,b,c}$ for the PWM. In mode II, average current control method is adopted where the difference of the dc bus voltage command V^*_{dc} and dc bus voltage V_{dc} is regulated by a PI or the proposed CFNN-AMF controller to produce the current command i^*_{bat} of the dc/dc converter. Then, the current command i^*_{bat} is divided by three for the three arms of the dc/dc converter, and the differences between the current commands and the sensed phase currents $i_{\text{bat }a}$, $i_{\text{bat }b}$, and $i_{\text{bat }c}$ are regulated via an individual PI controller to generate the control signal commands $V^*_{\text{con }a}$, $V^*_{\text{con }b}$, and $V^*_{\text{con }c}$ for the PWM.

For the three-level NPC inverter, it is controlled by the $dq0$-axis current control. The *d*-axis current control is responsible for the reactive power control by using the reactive power current command i^*_{do}. The *q*-axis current control is responsible for the active power control by using the active power current command i^*_{qo}. In mode I, the difference of the dc bus voltage command V^*_{dc} and dc bus voltage V_{dc} is regulated by a PI or CFNN-AMF controller to produce the dc bus current command i_{qv} for maintaining the constant dc bus voltage. In mode II, first, P^* and Q^* are determined according to the grid codes of the utilities, in which the lagging power factor is set as 0.9 for the PV inverter output when the grid voltage is 5% higher than the normal voltage. Then, the control loop of P regulates the control output i_{qp}, which is the active current command, through a PI controller; the control loop of Q regulates the control output i_{dq}, which is the reactive current command, also through a PI controller. Moreover, the *0*-axis current control is responsible for the balance of the upper half dc bus voltage V_{d1} and the lower half dc bus voltage V_{d2} by using a PI controller to generate the *0*-axis current command i_{0v}.

To develop the compensation function of the three-phase unbalanced currents under three-phase unbalanced load in grid-connected operation, three resistors R_a, R_b, and R_c are designed to be unbalanced and are connected with the grid of a distribution system. The resulted non-sinusoidal currents could deteriorate the power quality seriously in the distribution system. Therefore, the control strategy proposed in Fig. 1(b) can compensate the three-phase unbalanced currents caused by unbalanced loads R_a, R_b, and R_c. The three-phase load currents i_{al}, i_{bl}, and i_{cl} are detected and transferred to $dq0$-axis currents i_{dl}, i_{ql}, and i_{0l}, respectively, in the synchronous reference frame. Then, the dc components are extracted via two low-pass filters which the transfer functions are designed as follows [21]:

$$T(s) = \frac{k\omega^2}{s^2 + 2\xi\omega s + \omega^2} \tag{4}$$

where the gain $k = 1$, damping ratio $\xi = 0.7$, and angular cutoff frequency $\omega = 20\pi$ rad/s. The dc components are subtracted by i_{dl} and i_{ql} to generate dq-axis current harmonic components $\tilde{i}_{dl}$ and $\tilde{i}_{ql}$, and the i_{0l} is named as the zero-axis current harmonic component $\tilde{i}_{0l}$. The control current i_{qp} is added to the *q*-axis current harmonic component $\tilde{i}_{ql}$ to obtain the *q*-axis current command i^*_{qo}. The control current i_{dq} is added to the *d*-axis current harmonic component $\tilde{i}_{dl}$ to obtain the *d*-axis current command i^*_{do}, and the control current i_{0v} is added to the zero-axis current harmonic component $\tilde{i}_{0l}$ to obtain the axis current command i^*_{0o}. The individual difference between the current commands i^*_{do}, i^*_{qo}, i^*_{0o} and the current i_{do}, i_{qo}, i_{0o} is regulated via three PI controllers to generate the respective $dq0$-axis voltage commands V^*_q, V^*_d, V^*_0. Then, V^*_q, V^*_d, and V^*_0 are converted to voltage commands V^*_a, V^*_b, and V^*_c in *abc*-axis for SPWM by using the synchronous angle θ_i.

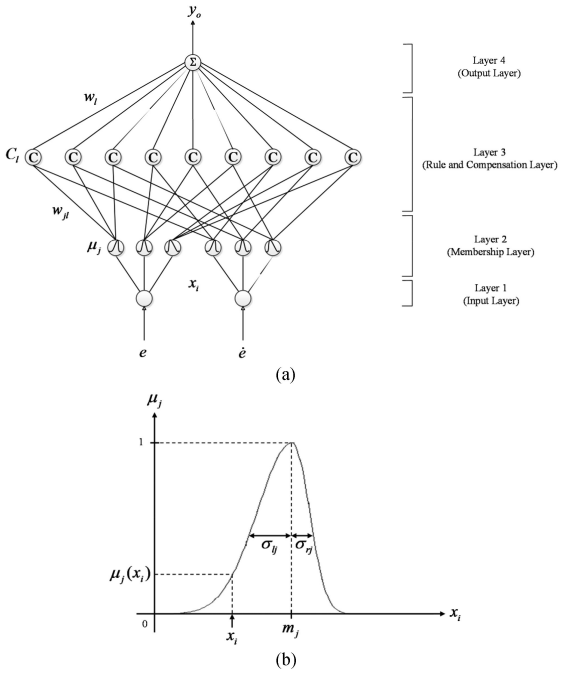

Fig. 2. Four-Layer CFNN-AMF. (a) Network structure. (b) Asymmetric Gaussian function.

III. Network Structure and Online Learning Algorithm for CFNN-AMF

A. Network Structure

A four-layer CFNN-AMF, which includes the input layer (layer 1), the membership layer (layer 2), the rule and compensation layer (layer 3), and the output layer (layer 4) with two inputs and one output, is shown in Fig. 2(a). Moreover, the signal propagation and the basic function of each layer are introduced in the following.

1) *Layer 1 (input layer):* In the input layer, the input and output nodes are represented as

$$\mathrm{net}_i(N) = e_i \tag{5}$$

$$x_i(N) = f_i(\mathrm{net}_i(N)) = \mathrm{net}_i(N) \quad i = 1,\ 2 \tag{6}$$

where x_i represents the *i*th input to the input layer; and *N* represents the *N*th iteration. In this study, the input variables are the tracking error, which is $e_1(N) = e = V_{\mathrm{dc}}^* - V_{\mathrm{dc}}$ for dc bus voltage control, and its derivative $e_2(N) = \dot{e}$.

2) *Layer 2 (membership layer):* In the membership layer, each node utilizes an asymmetric Gaussian function to realize the fuzzification operation in the CFNN-AMF as shown in Fig. 2(b). The node input and output of this layer are presented as

$$\mathrm{net}_j(N) = \begin{cases} -\dfrac{(x_i(N) - m_j(N))^2}{(\sigma_{lj}(N))^2}, & -\infty < x_i(N) \le m_j \\ -\dfrac{(x_i(N) - m_j(N))^2}{(\sigma_{rj}(N))^2}, & m_j < x_i(N) \le \infty \end{cases} \tag{7}$$

$$\mu_j(N) = f_j(\mathrm{net}_j(N)) = \exp(\mathrm{net}_j(N)), \quad j = 1, 2, \ldots, 6 \tag{8}$$

where $\mu_j(N)$ is the layer-2 node output; m_j is the mean of the asymmetric Gaussian function in the *j*th term associated with the *i*th input variable; and σ_{lj} and σ_{rj} are the left-hand-side and right-hand-side standard deviations of the asymmetric Gaussian function in the *j*th term associated with the *i*th input variable.

3) *Layer 3 (rule and compensation layer):* Nodes in this layer represent the precondition part of one fuzzy logic rule. The compensatory operator mentioned previously is adopted here to perform IF-condition matching of fuzzy rules. As a result, the output function of each inference node is

$$\mu_l = \prod_j^n w_{jl}\mu_j \tag{9}$$

$$\mathrm{net}_l(N) = (\mu_l)^{1-\gamma_l+\gamma_l/n} \qquad \gamma_l = [0,1] \tag{10}$$

$$C_l(N) = f_l(\mathrm{net}_l(N)) = \mathrm{net}_l(N), \quad l = 1, 2, \ldots, 9 \tag{11}$$

where $n = 2$; $\mu_l(N)$ is the input of rule layer; w_{jl} is the connective weight between the membership layer and the rule and compensation layer which is set to be 1; $\gamma_l \in [0,1]$ is called the compensatory degree; and $C_l(N)$ is the *l*th node output of the rule and compensation layer. When γ_l is tuned online as $\gamma_l(N)$, the compensatory operator becomes more adaptive. To ensure $\gamma_l \in [0,1]$, the compensatory degree γ_l is defined as $\gamma_l = \frac{{c_l}^2}{({c_l}^2+{d_l}^2)}$ [22], where parameters c_l and d_l will be trained real time.

4) *Layer 4 (output layer):* In the output layer, the node output is represented as

$$\mathrm{net}_o(N) = \sum_l w_l(N)C_l(N) \tag{12}$$

$$y_o(N) = f_o(\mathrm{net}_o(N)) = \mathrm{net}_o(N) \qquad o = 1 \tag{13}$$

where $y_o(N)$ is the output of the CFNN-AMF; w_l is the connective weight between the rule and compensation layer and the output layer, and $C_l(N)$ represents the *j*th input to the node of layer 4.

B. Online Learning Algorithms

To describe the online learning algorithm of the CFNN-AMF using supervised gradient decent method, the dc bus voltage control is taken for example. First, the energy function $E(N)$ is defined as

$$E(N) = \frac{1}{2}(V_{\mathrm{dc}}^* - V_{\mathrm{dc}})^2 = \frac{1}{2}e^2. \tag{14}$$

Then, the learning algorithm using the BP learning rule is described as follows:

1) *Layer 4:* The error term to be propagated is given by

$$\delta_o^4 = -\frac{\partial E}{\partial y_o(N)} = -\frac{\partial E}{\partial V_{\mathrm{dc}}}\frac{\partial V_{\mathrm{dc}}}{\partial y_o(N)} \cong e + \dot{e}. \tag{15}$$

The weight is updated by the amount

$$\Delta w_l = -\eta_1 \frac{\partial E}{\partial w_l} = -\eta_1 \frac{\partial E}{\partial y_o(N)} \frac{\partial y_o(N)}{\partial w_l} = \eta_1 \delta_o^4 C_l \quad (16)$$

where the factor η_1 is the learning rate. The connective weight w_l is updated according to the following equation:

$$w_l(N+1) = w_l(N) + \Delta w_l. \quad (17)$$

2) *Layer 3:* In this layer, the error terms to be propagated are given by

$$\delta_o^3 = -\frac{\partial E}{\partial C_l(N)} = -\frac{\partial E}{\partial y_o(N)} \frac{\partial y_o(N)}{\partial C_l(N)} = \delta_o^4 w_l. \quad (18)$$

$\gamma_l(N)$ is defined as follows:

$$\gamma_l(N) = \frac{{c_l}^2(N)}{{c_l}^2(N) + {d_l}^2(N)}. \quad (19)$$

The parameters $c_l(N)$ and $d_l(N)$ are updated by the amount

$$\begin{aligned}\Delta c_l &= -\eta_c \frac{\partial E}{\partial c_l(N)} = -\eta_c \frac{\partial E}{\partial r_l(N)} \frac{\partial \gamma_l(N)}{\partial c_l(N)} \\ &= -\eta_c \frac{\partial E}{\partial \gamma_l(N)} \frac{2c_l(N) d_l(N)^2}{\left(c_l(N)^2 + d_l(N)^2\right)^2} \\ &= \eta_c \Delta\gamma_l \frac{2c_l(N) d_l(N)^2}{\left(c_l(N)^2 + d_l(N)^2\right)^2} \end{aligned} \quad (20)$$

$$\begin{aligned}\Delta d_l &= -\eta_d \frac{\partial E}{\partial d_l(N)} = -\eta_d \frac{\partial E}{\partial r_l(N)} \frac{\partial \gamma_l(N)}{\partial d_l(N)} \\ &= -\eta_d \frac{\partial E}{\partial \gamma_l(N)} \frac{-2c_l(N)^2 d_l(N)}{\left(c_l(N)^2 + d_l(N)^2\right)^2} \\ &= \eta_d \Delta\gamma_l \frac{-2c_l(N)^2 d_l(N)}{\left(c_l(N)^2 + d_l(N)^2\right)^2} \end{aligned} \quad (21)$$

and

$$\begin{aligned}\Delta\gamma_l &= -\frac{\partial E}{\partial \gamma_l(N)} = -\frac{\partial E}{\partial C_l(N)} \frac{\partial C_l(N)}{\partial \gamma_l(N)} \\ &= \delta_o^3 \left(\frac{1}{n} - 1\right) \left(\prod_j w_{jl}\mu_j\right)^{1-\gamma_l + \frac{\gamma_l}{n}} \ln\left(\prod_j w_{jl}\mu_j\right) \end{aligned} \quad (22)$$

where the factors η_c and η_d are the learning rate of the parameter c_l and d_l, respectively. The parameters c_l, d_l and the compensatory degree are updated according to the following equation:

$$\begin{aligned}c_l(N+1) &= c_l(N) + \Delta c_l \\ &= c_l(N) + \eta_c \left\{\frac{2c_l(N) {d_l}^2(N)}{\left[{c_l}^2(N) + {d_l}^2(N)\right]^2}\right\} \Delta\gamma_l \end{aligned} \quad (23)$$

$$\begin{aligned}d_l(N+1) &= d_l(N) + \Delta d_l \\ &= d_l(N) - \eta_d \left\{\frac{2{c_l}^2(N) d_l(N)}{\left[{c_l}^2(N) + {d_l}^2(N)\right]^2}\right\} \Delta\gamma_l \end{aligned} \quad (24)$$

$$\gamma_l(N+1) = \frac{{c_l}^2(N+1)}{{c_l}^2(N+1) + {d_l}^2(N+1)}. \quad (25)$$

3) *Layer 2:* The error term to be propagated in this layer is given by

$$\begin{aligned}\delta_o^2 &= -\frac{\partial E}{\partial net_j(N)} = -\frac{\partial E}{\partial C_l(N)} \frac{\partial C_l(N)}{\partial \mu_j(N)} \frac{\partial \mu_l(N)}{\partial \mathrm{net}_j(N)} \\ &= \sum_j \delta_o^3 \mu_l \left(1 - \gamma_l + \frac{\gamma_l}{n}\right) \left(\prod_j w_{jl}\mu_j\right)^{-\gamma_l + \frac{\gamma_l}{n}}. \end{aligned} \quad (26)$$

Applying the chain rule, the update law of mean of the asymmetric Gaussian function is

$$\begin{aligned}\Delta m_j &= -\eta_2 \frac{\partial E}{\partial m_j} = -\eta_2 \frac{\partial E}{\partial \mu_j(N)} \frac{\partial \mu_j(N)}{\partial m_j} \\ &= \begin{cases} 2\eta_2 \delta_o^2 \frac{(x_i(N) - m_j(N))}{(\sigma_{lj}(N))^2}, & -\infty < x_i(N) \le m_j \\ 2\eta_2 \delta_o^2 \frac{(x_i(N) - m_j(N))}{(\sigma_{rj}(N))^2}, & m_j < x_i(N) \le \infty \end{cases}. \end{aligned} \quad (27)$$

The update rules of σ_{lj} and σ_{rj} are

$$\begin{aligned}\Delta\sigma_{lj} &= -\eta_3 \frac{\partial E}{\partial \sigma_{lj}} = -\eta_3 \frac{\partial E}{\partial \mu_{lj}(N)} \frac{\partial \mu_{lj}(N)}{\partial \sigma_{lj}} \\ &= 2\eta_3 \delta_o^2 \frac{(x_i - m_j)^2}{(\sigma_{lj})^3} \end{aligned} \quad (28)$$

$$\begin{aligned}\Delta\sigma_{rj} &= -\eta_4 \frac{\partial E}{\partial \sigma_{rj}} = -\eta_4 \frac{\partial E}{\partial \mu_{rj}(N)} \frac{\partial \mu_{rj}(N)}{\partial \sigma_{rj}} \\ &= 2\eta_4 \delta_o^2 \frac{(x_i - m_j)^2}{(\sigma_{rj})^3} \end{aligned} \quad (29)$$

where the factors η_2, η_3, and η_4 are the learning rates. The mean and left-hand-side and right-hand-side standard deviations of the AMFs are updated according to the following equations:

$$m_j(N+1) = m_j(N) + \Delta m_j \quad (30)$$

$$\sigma_{lj}(N+1) = \sigma_{lj}(N) + \Delta\sigma_{lj} \quad (31)$$

$$\sigma_{rj}(N+1) = \sigma_{rj}(N) + \Delta\sigma_{rj}. \quad (32)$$

The exact calculation of the Jacobian of the system $\partial V_{\mathrm{dc}}/\partial y_o(N)$ is difficult to be determined due to the unknown dynamics of the PV system. To overcome this problem, a delta

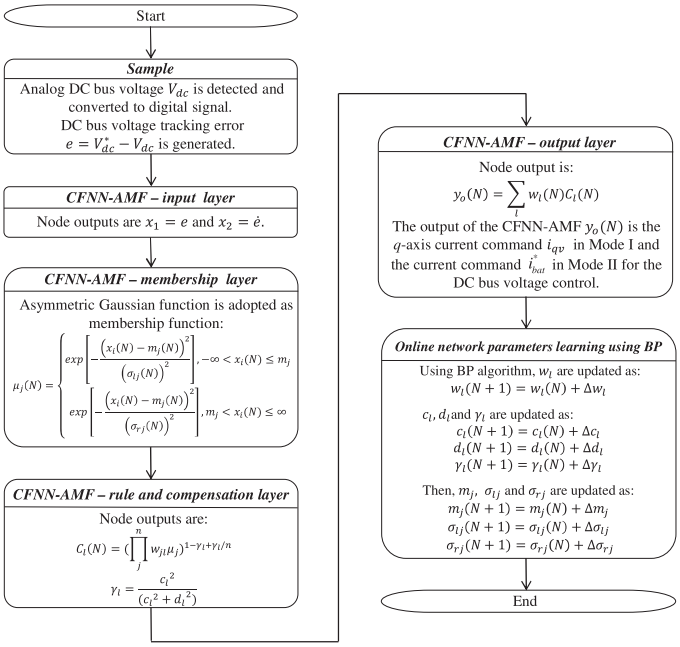

Fig. 3. Flowchart of dc bus voltage control using the proposed CFNN-AMF.

adaptation law is adopted as follows [23]:

$$\delta_o^4 \cong (V_{\rm dc}^* - V_{\rm dc}) + (\dot{V}_{\rm dc}^* - \dot{V}_{\rm dc}) = e + \dot{e}. \tag{33}$$

C. Procedure of DC Bus Voltage Control

The flowchart of dc bus voltage control using the proposed CFNN-AMF is provided in Fig. 3 and described as follows.

1) *Sample:* The analog dc bus voltage signal is detected by a voltage sensor circuit and converted to digital signal via an analog-to-digital converter in the DSP. Then, the dc bus voltage tracking error $e = V_{\rm dc}^* - V_{\rm dc}$ is generated and sent to the proposed CFNN-AMF control.
2) *CFNN-AMF input layer:* The input variables of the CFNN-AMF are e and $\dot{e}$. In the input layer, the node outputs are $x_1 = e$ and $x_2 = \dot{e}$ and sent to the membership layer.
3) *CFNN-AMF membership layer:* The asymmetric Gaussian function is adopted as the membership functions and the outputs are $\mu_j(N)$. Then, the outputs $\mu_j(N)$ are sent to the rule and compensation layer, which represent the precondition part of one fuzzy logic rule.
4) *CFNN-AMF rule and compensation layer:* The compensatory operator is adopted here to perform IF-condition matching of fuzzy rules. The outputs are $C_l(N)$ and sent to the output layer.
5) *CFNN-AMF output layer:* The node performs the summation operation and the output is given as $y_o(N)$. Moreover, the output of the CFNN-AMF $y_o(N)$ is the q-axis current command i_{qv} in mode I and the current command $i_{\rm bat}^*$ in mode II for the dc bus voltage control in the three-level NPC inverter and interleaved dc/dc converter, respectively.
6) *Online network parameters learning using BP:* The online parameters learning is achieved by online tuning of the connective weights $w_l(N)$ between the output layer and the rule and compensation layer, the parameters $c_l(N)$, $d_l(N)$, and $r_l(N)$ in the rule and compensation layer, and the mean $m_j(N)$ and left-hand-side $\sigma_{lj}(N)$ and right-hand-side $\sigma_{rj}(N)$ standard deviations of the AMFs in the membership layer using the BP algorithm.

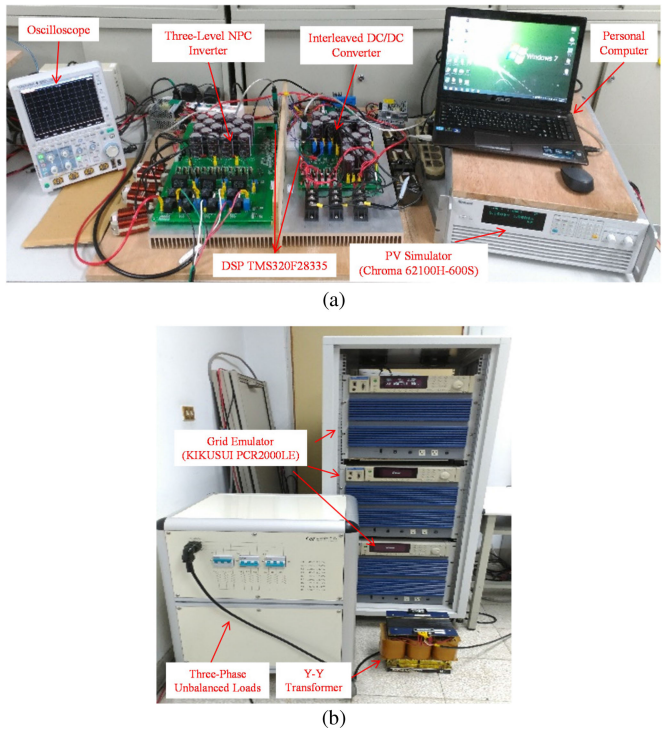

Fig. 4. Photos of experimental setup. (a) Interleaved dc/dc converter, three-level NPC inverter, and PV simulator. (b) Three-Phase unbalanced loads, Y-Y transformer, and grid emulator.

IV. Experimental Setup and Experimentation

A. Experimental Setup

The photos of the PV power system, including two DSP TMS320F28335 control boards, are shown in Fig. 4(a) and (b). The interleaved dc/dc converter, three-level NPC inverter, and PV simulator are shown in Fig. 4(a). Three-phase unbalanced loads, Y-Y transformer, and grid emulator are shown in Fig. 4(b). For the dc/dc converter, the values of input capacitor, three filter inductors, and output capacitor are 1175 μF, 0.52 mH, and 1175 μF, respectively. For the dc/ac inverter, the values of capacitors of dc bus, and the values of inductors and capacitors of three output filters are 3760 μF, 1.6 mH, and 10 μF, respectively. The cutoff frequency f_c of the output filter is 1.258 kHz. Moreover, the dc bus voltage command $V_{\rm dc}^*$ is set at 450 V. Furthermore, the switching frequency of the interleaved dc/dc converter and three-level NPC inverter are both set to be 16 kHz. In addition, the sampling frequency 1 kHz is adopted for the control algorithms of both stages.

In the experimentation, two unbalanced load conditions are given in the following: R_a, R_b, and R_c are 80, 40, and 100 Ω, respectively, in load 1; R_a, R_b, and R_c are 40, 20, and 60 Ω, respectively in load 2. Two test cases are configured as follows: In case 1, three-phase voltages of the inverter V_a, V_b, and V_c

are set at 1 p.u. and PV power system is operated at mode I (MPPT mode); inverter output power is set at 2 kW; and the load conditions are switched from load 1 to load 2. In case 2, three-phase voltages of the inverter V_a, V_b, and V_c are set at 1.05 p.u. and PV power system is operated at mode II (smart inverter mode); P^* and Q^* are set at 1.8 kW and -871 VAR with lagging power factor 0.9; and the load conditions are switched from load 1 to load 2. In addition, a three-phase unbalanced current ratio U_R is defined in the following to compare the compensation performance of the PV power system:

$$U_R = \frac{\text{Max}\ (i_{ag},\ i_{bg},\ i_{cg}) - \text{Min}\ (i_{ag},\ i_{bg},\ i_{cg})}{\text{Average}\ (i_{ag},\ i_{bg},\ i_{cg})} 100\% \quad (34)$$

where $\text{Max}\,(i_{ag}, i_{bg}, i_{cg})$ is the maximum RMS current of the three-phase currents i_{ag}, i_{bg}, and i_{cg} of the grid; $\text{Min}\,(i_{ag}, i_{bg}, i_{cg})$ is the minimum RMS current of the three-phase currents i_{ag}, i_{bg}, and i_{cg}; and $\text{Average}\,(i_{ag}, i_{bg}, i_{cg})$ is the average RMS current of the three-phase currents i_{ag}, i_{bg}, and i_{cg}. The lesser the value of the three-phase unbalanced current ratio U_R is, the more superior the compensation performance is.

B. Experimentation

The experimental results of the PV power system under unbalanced load conditions without using the compensation function of the three-phase unbalanced currents at case 1 and adopting the PI controller for the control of DC bus voltage are shown in Fig. 5. The responses of the inverter voltage V_a, the three-phase currents of the dc/ac inverter i_{ao}, i_{bo}, i_{co}, the three-phase currents of the unbalanced load i_{al}, i_{bl}, and i_{cl}, and the three-phase currents of the grid i_{ag}, i_{bg}, and i_{cg} are shown in Fig. 5(a). The dc bus voltage V_{dc} and the active and reactive powers P and Q are shown in Fig. 5(b). From the experimental results shown in Fig. 5(a), owing to the unbalanced load and the absence of the compensation function, the three-phase currents i_{ag}, i_{bg}, and i_{cg} of the grid are unbalanced with larger values of U_R66.4% for load 1 and 63.5% for load 2. Moreover, in order to verify the effectiveness of the proposed PV power system under unbalanced load conditions, the experimental results using the compensation function of the three-phase unbalanced currents at case 1 and adopting the PI controller for the control of dc bus voltage are provided in Fig. 6 to demonstrate the compensation performance. The responses of the inverter voltage V_a, the three-phase currents of the dc/ac inverter i_{ao}, i_{bo}, and i_{co}, the three-phase currents of the unbalanced load i_{al}, i_{bl}, and i_{cl}, and the three-phase currents of the grid i_{ag}, i_{bg}, and i_{cg} are shown in Fig. 6(a). The dc bus voltage V_{dc} and the active and reactive powers P and Q are shown in Fig. 6(b). The main objective of the compensation function is to make the three-phase currents of the grid i_{ag}, i_{bg}, and i_{cg} be balanced. Hence, from the experiment shown in Fig. 6(a), the three-phase currents of the grid i_{ag}, i_{bg}, and i_{cg} can be compensated to be more balanced with smaller values of U_R 8.47% for load 1 and 27.34% for load 2. The settling time is 0.33 s and the undershoot-to-overshoot voltage is 15.2 V for the dc bus voltage V_{dc} shown in Fig. 6(b). Furthermore, the experimental results using the compensation

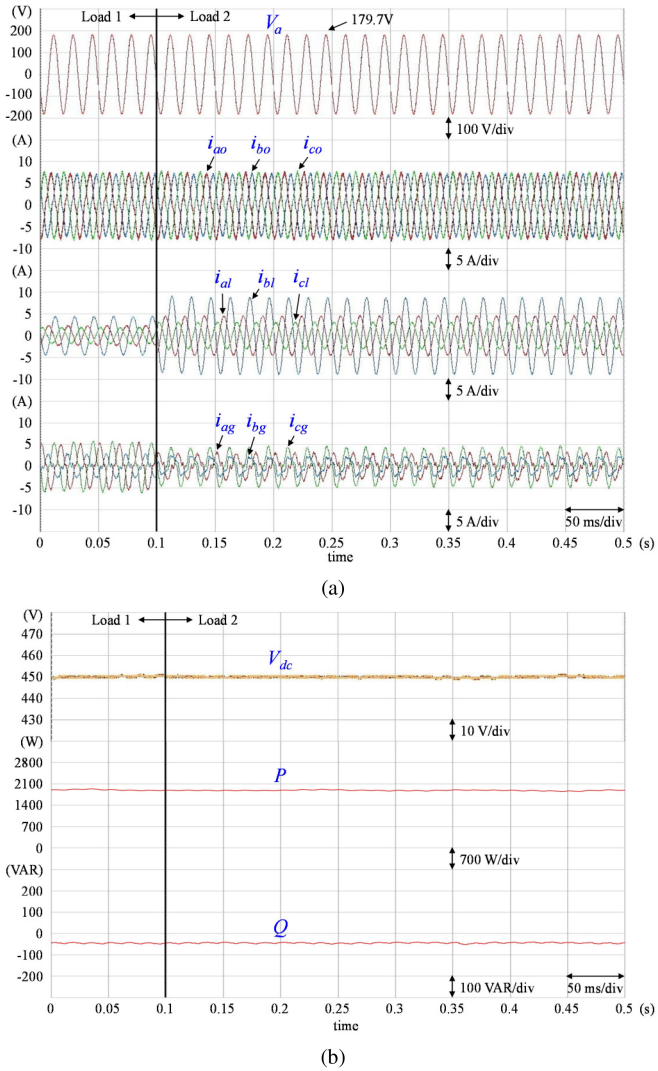

Fig. 5. Case 1 without three-phase unbalanced current compensation and with PI dc bus voltage controller. (a) Responses of inverter voltage, three-phase currents of inverter, three-phase currents of unbalanced loads, and three-phase currents of grid. (b) Responses of dc bus voltage and active and reactive powers.

function of the three-phase unbalanced currents at case 1 and adopting the CFNN-AMF controller for the control of dc bus voltage are shown in Fig. 7. The responses of the inverter voltage V_a, the three-phase currents of the dc/ac inverter i_{ao}, i_{bo}, and i_{co}, the three-phase currents of the unbalanced load i_{al}, i_{bl}, and i_{cl}, and the three-phase currents of the grid i_{ag}, i_{bg}, and i_{cg} are shown in Fig. 7(a). The dc bus voltage $V_{\text{dc}}$and the active and reactive powers P and Q are shown in Fig. 7(b). From the experimental results, the three-phase currents of the grid i_{ag}, i_{bg}, and i_{cg} can be compensated to be more balanced with smaller values of U_R 8.13% for load 1 and 24.16% for load 2 as shown in Fig. 7(a). In addition, for the dc bus voltage V_{dc}, the settling time is 0.28 s and the undershoot-to-overshoot voltage is 13.6 V as shown in Fig. 7(b).

The experimental results of the PV power system under unbalanced load conditions without using the compensation function of the three-phase unbalanced currents at case 2 and adopting the PI controller for the control of dc bus voltage are shown in

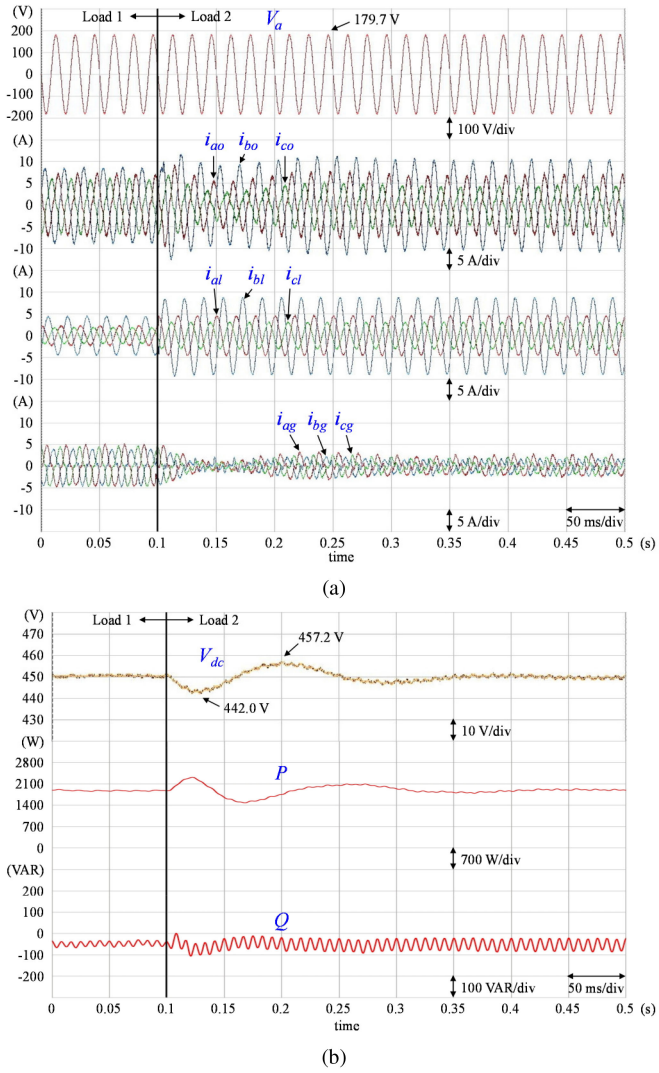

Fig. 6. Case 1 with three-phase unbalanced current compensation and with PI DC bus voltage controller. (a) Responses of inverter voltage, three-phase currents of inverter, three-phase currents of unbalanced loads, and three-phase currents of grid. (b) Responses of dc bus voltage and active and reactive powers.

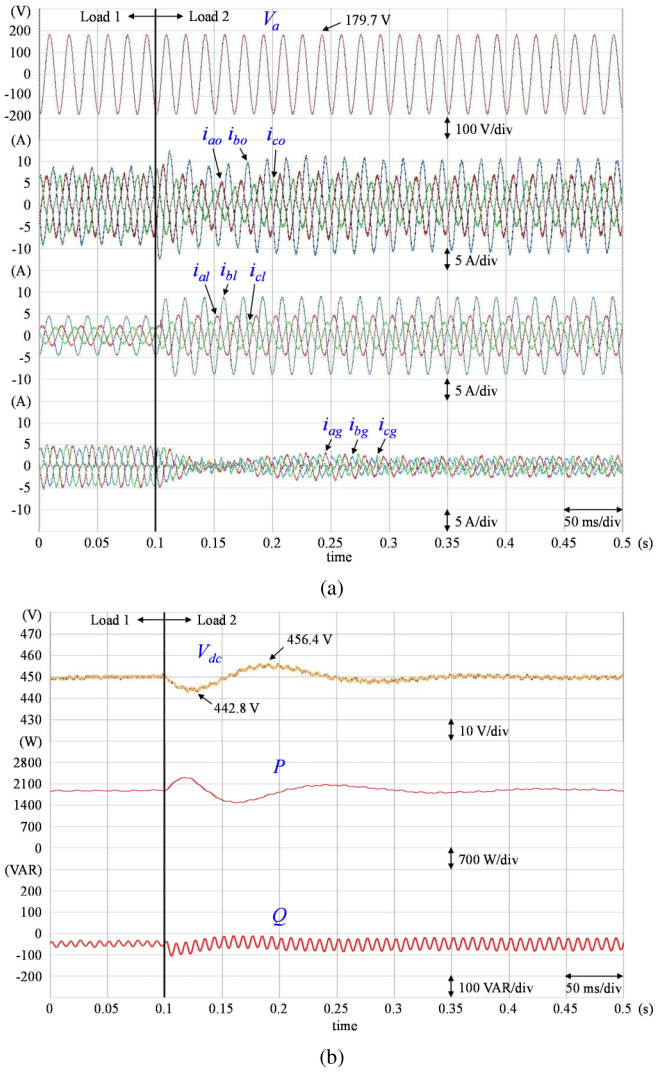

Fig. 7. Case 1 with three-phase unbalanced current compensation and with CFNN-AMF dc bus voltage controller. (a) Responses of inverter voltage, three-phase currents of inverter, three-phase currents of unbalanced loads, and three-phase currents of grid. (b) Responses of dc bus voltage and active and reactive powers.

Fig. 8. The responses of the inverter voltage V_a, the three-phase currents of the dc/ac inverter i_{ao}, i_{bo}, and i_{co}, the three-phase currents of the unbalanced load i_{al}, i_{bl}, and i_{cl}, and the three-phase currents of the grid i_{ag}, i_{bg}, and i_{cg} are shown in Fig. 8(a). The dc bus voltage $V_{\rm dc}$and the active and reactive powers P and Q are shown in Fig. 8(b). From the experimental results shown in Fig. 8(a), owing to the unbalanced load and the absence of the compensation function, the three-phase currents i_{ag}, i_{bg}, and i_{cg} of the grid are unbalanced with larger values of U_R 60.74% for load 1 and 30.12% for load 2. Moreover, the experimental results using the compensation function of the three-phase unbalanced currents at case 2 and adopting the PI controller for the control of dc bus voltage are provided in Fig. 9 to demonstrate the compensation performance. The responses of the inverter voltage V_a, the three-phase currents of the dc/ac inverter i_{ao}, i_{bo}, and i_{co}, the three-phase currents of the unbalanced load i_{al}, i_{bl}, and i_{cl}, and the three-phase currents of the grid i_{ag}, i_{bg}, and i_{cg} are shown in Fig. 9(a). The dc bus voltage $V_{\rm dc}$and the active and reactive powers P and Q are shown in Fig. 9(b). From the experiment shown in Fig. 9(a), the three-phase currents of the grid i_{ag}, i_{bg}, and i_{cg} can be compensated to be more balanced with smaller values of U_R 7.32% for load 1 and 3.04% for load 2. For the dc bus voltage $V_{\rm dc}$, the settling time is 0.14 s and the undershoot-to-overshoot voltage is 7.4 V as shown in Fig. 9(b). Furthermore, the experimental results using the compensation function of the three-phase unbalanced currents at case 2 and adopting the CFNN-AMF controller for the control of dc bus voltage are shown in Fig. 10. The responses of the inverter voltage V_a, the three-phase currents of the dc/ac inverter i_{ao}, i_{bo}, and i_{co}, the three-phase currents of the unbalanced load i_{al}, i_{bl}, and i_{cl}, and the three-phase currents of the grid i_{ag}, i_{bg}, and i_{cg} are shown in Fig. 10(a). The dc bus voltage $V_{\rm dc}$and the active and reactive powers P and Q are shown in Fig. 10(b). Owing to the excellent intelligent control properties of the proposed

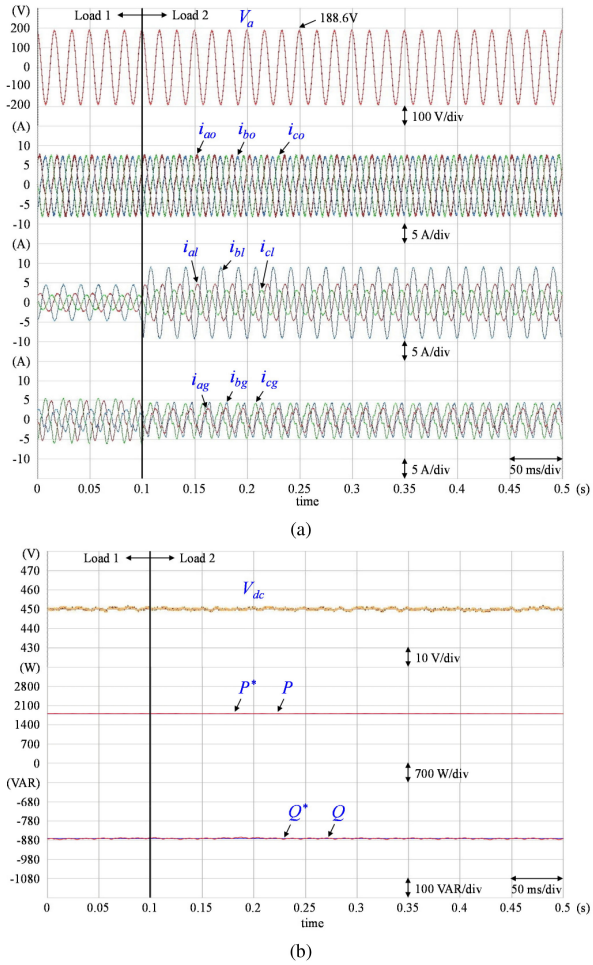

Fig. 8. Case 2 without three-phase unbalanced current compensation and with PI dc bus voltage controller. (a) Responses of inverter voltage, three-phase currents of inverter, three-phase currents of unbalanced loads, and three-phase currents of grid. (b) Responses of dc bus voltage and active and reactive powers.

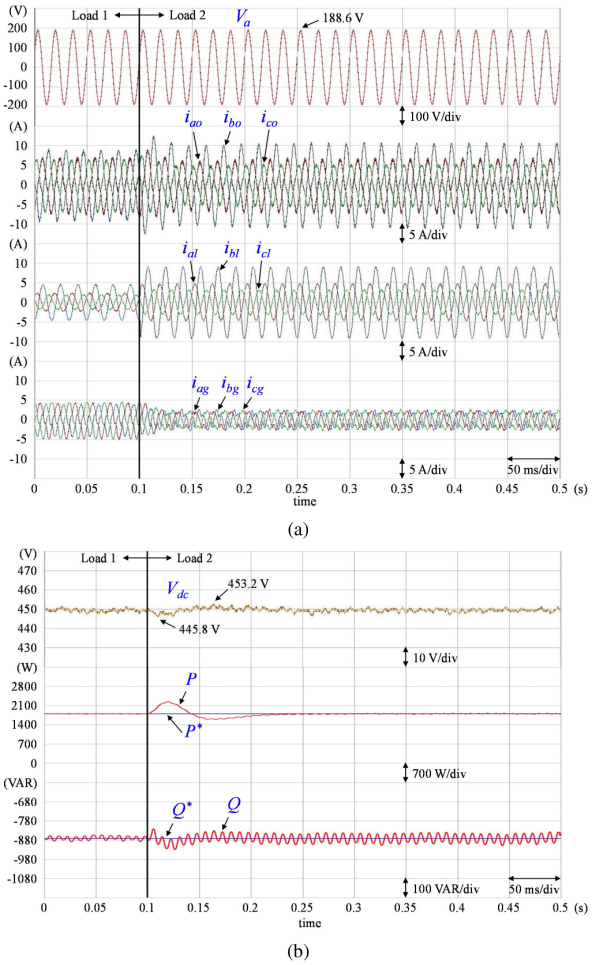

Fig. 9. Case 2 with three-phase unbalanced current compensation and with PI dc bus voltage controller. (a) Responses of inverter voltage, three-phase currents of inverter, three-phase currents of unbalanced loads, and three-phase currents of grid. (b) Responses of dc bus voltage and active and reactive powers.

CFNN-AMF controller, the three-phase currents of the grid i_{ag}, i_{bg}, and i_{cg} are compensated to be much more balanced with smaller values of U_R 6.9% for load 1 and 3.01% for load 2 as shown in Fig. 10(a). In addition, for the dc bus voltage $V_{\rm dc}$, the settling time is 0.05 s and the undershoot-to-overshoot voltage is 6.4 V as shown in Fig. 10(b).

In terms of two dc bus voltage controller and without and with using compensation function, the three-phase unbalanced current ratio U_R is compared in Table I. Moreover, in terms of two dc bus voltage controller and the changing of load conditions, the settling time and the undershoot-to-overshoot voltage are compared in Tables II and III, respectively, for test conditions case 1 and case 2. Since the control performance of the dc bus voltage using the CFNN-AMF controller of the PV power system under unbalanced load variation condition is improved comparing with using the PI controller, all the three-phase unbalanced current ratio U_R, the settling time, and the undershoot-to-overshoot voltage of the dc bus voltage $V_{\rm dc}$ are reduced at both test cases. However, since in case 1, the SPWM of the inverter has to handle the dc bus control and the three-phase unbalanced currents compensation simultaneously, the control performance of both the PI and CFNN-AMF controller are inferior to case 2 where the dc bus voltage control is processed by the PWM of the converter.

The execution or compute time of the "C" program in the TMS320F28335 32-bit floating-point DSP with 150 MHz can be obtained by the clock tool of TI Code Composer Studio v6 program editing interface. The total operation cycles and total execution time of the PV power system using PI and the proposed CFNN-AMF controllers are compared in Table IV. The total operation cycles and total execution time for the proposed CFNN-AMF are 62 156 cycles and 0.414 ms, respectively. Though comparing with the PI controller, there is extra computational delay using the proposed CFNN-AMF controller, the total execution time of the proposed CFNN-AMF is still less than 1 ms, which is the sampling interval of the control loop. Moreover, the computation complexity of the proposed CFNN-AMF controller can be evaluated by the number of steps required to compute the output of the CFNN-AMF controller and the online learning algorithm. A step is one of the following operations: addition, subtraction, multiplication, division, and comparison of two numbers. The steps of each layer in the CFNN-AMF are calculated according to (5)–(13). The numbers of steps of layer 1 to layer 4 are 0, 54, 129, and 18. Therefore, the steps of

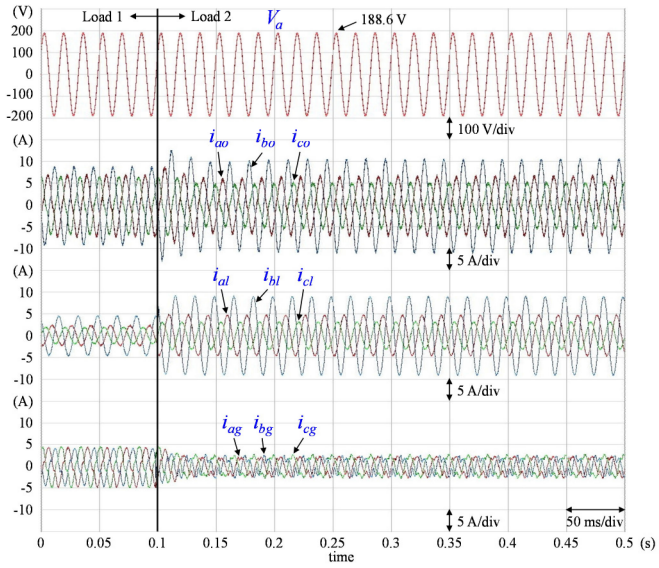

Fig. 10. Case 2 with three-phase unbalanced current compensation and with CFNN-AMF dc bus voltage controller. (a) Responses of inverter voltage, three-phase currents of inverter, three-phase currents of unbalanced loads, and three-phase currents of grid. (b) Responses of dc bus voltage and active and reactive powers.

TABLE I
COMPARISON OF THREE-PHASE UNBALANCED CURRENT RATIO U_R AT VARIOUS TEST CONDITIONS

DC Bus Voltage Controller	Using Unbalance Compensation	Unbalanced Current Ratio (%)			
		Mode I		Mode II	
		Load 1	Load 2	Load 1	Load 2
PI	No	66.4	63.5	60.74	30.12
PI	Yes	8.47	27.34	7.32	3.04
CFNN-AMF	Yes	8.13	24.16	6.9	3.01

TABLE II
COMPARISON OF SETTLING TIME AND UNDERSHOOT-TO-OVERSHOOT VOLTAGE AT VARIOUS TEST CONDITIONS OF CASE 1

DC Bus Voltage Controllers	Settling Time (s)		Undershoot to Overshoot (V)	
	Load 1 → Load 2	Load 2 → Load 1	Load 1 → Load 2	Load 2 → Load 1
PI	0.33	0.35	15.2	15.1
CFNN-AMF	0.28	0.29	13.6	13.6

TABLE III
COMPARISON OF SETTLING TIME AND UNDERSHOOT-TO-OVERSHOOT VOLTAGE AT VARIOUS TEST CONDITIONS OF CASE 2

DC Bus Voltage Controllers	Settling Time (s)		Undershoot to Overshoot (V)	
	Load 1 → Load 2	Load 2 → Load 1	Load 1 → Load 2	Load 2 → Load 1
PI	0.14	0.12	7.4	7.2
CFNN-AMF	0.05	0.06	6.4	6.4

TABLE IV
EXECUTION TIME OF PV POWER SYSTEM USING PI AND PROPOSED CFNN-AMF CONTROLLERS

Controllers	PI	Proposed CFNN-AMF
Total Operation Cycles	88	62156
Execution Time	0.587 us	0.414 ms

signal propagation in the CFNN-AMF control scheme are 201. Similarly, the number of the total steps of the online learning algorithm is 563, which is calculated according to (17), (23)–(25), and (30)–(32). Subsequently, the proposed CFNN-AMF controller required 764 steps for the complete algorithm.

V. CONCLUSION

The development and implementation of a two-stage PV power system without the augmentation of APF to compensate the three-phase unbalanced currents are successfully presented in this study. The control architectures of the two-stage PV power system can fall into two categories: mode I is the MPPT mode; and mode II is the smart inverter mode, in which the output active and reactive powers of the PV inverter are predetermined by a lagging power factor according to grid codes of the utilities. Moreover, in order to improve the control performance of the dc bus voltage of the PV power system under unbalanced load variation condition, an online-trained CFNN-AMF is proposed for the dc bus voltage control. The network structure and online learning algorithms of the proposed CFNN-AMF have been presented in detail. Furthermore, from the experimental results of the PV power system using the proposed CFNN-AMF controller, the three-phase unbalanced grid currents compensation and the control performance of the dc bus voltage are much improved due to the robust fuzzy control and online training capability of the CFNN-AMF controller.

The major contributions of this study are: 1) the successful development of a two-stage PV power system to compensate the three-phase unbalanced grid currents; 2) the successful development of the proposed online-trained CFNN-AMF controller for the dc bus voltage control; and 3) the successful implementation of a DSP-based two-stage PV power system with the functions of smart inverter and unbalanced grid currents compensation.

REFERENCES

[1] S. Kouro, J. I. Leon, D. Vinnikov, and L. G. Franquelo, "Grid-Connected photovoltaic systems: An overview of recent research and emerging PV converter technology," *IEEE Ind. Electron. Mag.*, vol. 9, no. 1, pp. 47–67, Mar. 2015.

[2] S. Weckx and J. Driesen, "Optimal local reactive power control by PV inverters," *IEEE Trans. Sustain. Energy*, vol. 7, no. 4, pp. 1624–1633, Oct. 2016.
[3] G. Mokhtari, A. Ghosh, G. Nourbakhsh, and G. Ledwich, "Smart robust resources control in LV network to deal with voltage rise issue," *IEEE Trans. Sustain. Energy*, vol. 4, no. 4, pp. 1043–1050, Oct. 2013.
[4] Y. Q. Zhang and A. Kandel, "Compensatory neurofuzzy systems with fast learning algorithms," *IEEE Trans. Neural Netw.*, vol. 9, no. 1, pp. 83–105, Jan. 1998.
[5] H. Seker, D. E. Evans, N. Aydin, and E. Yazgan, "Compensatory fuzzy neural networks-based intelligent detection of abnormal neonatal cerebral Doppler ultrasound waveforms," *IEEE Trans. Inf. Technol. Biomed.*, vol. 5, no. 3, pp. 187–194, Sep. 2001.
[6] C. J. Lin and C. H. Chen, "Identification and prediction using recurrent compensatory neuro-fuzzy systems," *Fuzzy Sets Syst.*, vol. 150, no. 2, pp. 307–330, Mar. 2005.
[7] F. J. Lin, Y. C. Hung, J. C. Hwang, and M. T. Tsai, "Fault-Tolerant control of a six-phase motor drive system using a Takagi-Sugeno-Kang type fuzzy neural network with asymmetric membership function," *IEEE Trans. Power Electron.*, vol. 28, no. 7, pp. 3557–3572, Jul. 2013.
[8] Y. C. Hung, F. J. Lin, J. C. Hwang, J. K. Chang, and K. C. Ruan, "Wavelet fuzzy neural network with asymmetric membership function controller for electric power steering system via improved differential evolution," *IEEE Trans. Power Electron.*, vol. 30, no. 4, pp. 2350–2362, Apr. 2015.
[9] J. Miret, L. Garcia de Vicuna, M. Castilla, J. Matas, and J. Guerrero, "Design of an analog quasi-steady-state nonlinear current-mode controller for single-phase active power filter," *IEEE Trans. Ind. Electron.*, vol. 56, no. 12, pp. 4872–4881, Dec. 2009.
[10] P. Lohia, M. K. Mishra, K. Karthikeyan, and K. Vasudevan, "A minimally switched control algorithm for three-phase four-leg VSI topology to compensate unbalanced and nonlinear load," *IEEE Trans. Power Electron.*, vol. 23, no. 4, pp. 1935–1944, Jul. 2008.
[11] B. Kedjar and K. Al-Haddad, "DSP-Based implementation of an LQR with integral action for a three-phase three-wire shunt active power filter," *IEEE Trans. Ind. Electron.*, vol. 56, no. 8, pp. 2821–2828, Aug. 2009.
[12] P. Acuna, L.Moran, M. Rivera, J. Dixon, and J. Rodriguez, "Improved active power filter performance for renewable power generation systems," *IEEE Trans. Power Electron.*, vol. 29, no. 2, pp. 687–694, Feb. 2014.
[13] R. R. Pereira, C. H. da Silva, L. E. B. da Silva, G. Lambert-Torres, and J. O. P. Pinto, "New strategies for application of adaptive filters in active power filters," *IEEE Trans. Ind. Appl.*, vol. 47, no. 3, pp. 1136–1141, May/Jun. 2011.
[14] M. A. Mulla, C. Rajagopalan, and A. Chowdhury, "Compensation of three-phase diode rectifier with capacitive filter working under unbalanced supply conditions using series hybrid active power filter," *IET Power Electron.*, vol. 7, no. 6, pp. 1566–1577, Jun. 2014.
[15] M. Cirrincione, M. Pucci, G. Vitale, and A. Miraoui, "Current harmonic compensation by a single-phase shunt active power filter controlled by adaptive neural filtering," *IEEE Trans. Ind. Electron.*, vol. 56, no. 8, pp. 3128–3143, Aug. 2009.
[16] P. Jintakosonwit, H. Fujita, and H. Akagi, "Control and performance of a fully-digital-controlled shunt active filter for installation on a power distribution system," *IEEE Trans. Power Electron.*, vol. 17, no. 1, pp. 132–140, Jan. 2002.
[17] T. Mannen and H. Fujita, "Dynamic control and analysis of dc-capacitor voltage fluctuations in three-phase active power filters," *IEEE Trans. Power Electron.*, vol. 31, no. 9, pp. 6710–6718, Sep. 2016.
[18] S. Dusmez, A. Hasanzadeh, and A. Khaligh, "Comparative analysis of bidirectional three-level dc–dc converter for automotive applications," *IEEE Trans. Ind. Electron.*, vol. 62, no. 5, pp. 3305–3315, May 2015.
[19] H. Kosai, J. Scofield, S. McNeal, B. Jordan, and B. Ray, "Design and performance evaluation of a 200 °C interleaved boost converter," *IEEE Trans. Power Electron.*, vol. 28, no. 4, pp. 1691–1699, Apr. 2013.
[20] Z. Zhang, O. C. Thomsen, and M. A. E. Andersen, "Discontinuous PWM modulation strategy with circuit-level decoupling concept of three level neutral-point clamped (NPC) inverter," *IEEE Trans. Ind. Electron.*, vol. 60, no. 5, pp. 1897–1906, May 2013.
[21] K. H. Tan, F. J. Lin, and J. H. Chen, "Three-Phase four-leg inverter-based active power filter for unbalanced currents compensation using Petri probabilistic fuzzy neural network," *Energies*, vol. 10, pp. 1–17, Dec. 2017.
[22] C. S. Ouyang and S. J. Lee, "An improved learning algorithm for rule refinement in neuro-fuzzy modeling," in *Proc. 3rd Int. Conf. Knowl.-Based Intell. Inf. Eng. Syst.*, 1999, pp. 238–241.
[23] F. J. Lin, I. F. Sun, K. J. Yang, and J. K. Chang, "Recurrent fuzzy neural cerebellar model articulation network fault-tolerant control of six-phase PMSM position servo drive," *IEEE Trans. Fuzzy Syst.*, vol. 24, no. 1, pp. 153–167, Feb. 2016.

Faa-Jeng Lin (M'93–SM'99–F'17) received the B.S. and M.S. degrees in electrical engineering from National Cheng Kung University, Tainan, Taiwan, in 1983 and 1985, respectively, and the Ph.D. degree in electrical engineering from National Tsing Hua University, Hsinchu, Taiwan, in 1993.

He is currently a Chair Professor with the Department of Electrical Engineering, National Central University, Taoyuan, Taiwan. His research interests include ac motor drives, power electronics, renewable energies, smart grids, and intelligent and nonlinear control theories. His work has been widely cited. Several of his papers have helped to establish research areas such as fuzzy neural network control of motor drives and motion control systems, and resonant converters for piezoceramic motor drives.

Dr. Lin is an Associate Editor of the IEEE TRANSACTIONS ON FUZZY SYSTEMS and the IEEE TRANSACTIONS ON POWER ELECTRONICS. He is an IET Fellow. He received the Outstanding Research Awards from the National Science Council, Taiwan, in 2004, 2010, and 2013, respectively, and the Outstanding Professor of Engineering Award from the Chinese Institute of Engineers, Taiwan, in 2016.

Kuang-Hsiung Tan received the B.S., M.S., and Ph.D. degrees in electrical and electronic engineering from the Chung Cheng Institute of Technology (CCIT), National Defense University (NDU), Taoyuan, Taiwan, in 2002, 2007, and 2013, respectively.

He has been a member of the faculty with CCIT, NDU, where he is currently an Associate Professor with the Department of Electrical and Electronic Engineering. His teaching and research interests include power electronics, power quality, microgrid system, and intelligent control.

Yu-Kai Lai was born in Taichung City, Taiwan, in 1993. He received the B.S. degree in electrical engineering from the National Formosa University, Yunlin, Taiwan, in 2017, and the M.S. degree in electrical engineering from the National Central University, Taoyuan, Chungli, Taiwan, in 2017 and 2018, respectively.

His research interests include PV systems and intelligent control.

Wen-Chou Luo was born in Miaoli County, Taiwan, in 1994. He received the B.S. degree in electrical engineering from the National United University, Miaoli, in 2017. He is currently working toward the M.S. degree with the National Central University, Taoyuan, Chungli, Taiwan.

His research interests include active PV systems, intelligent control, and power electronics.